Ferroelectric phase transition in a 1*T* monolayer of $MoTe_2$: A first-principles study

Li-Bin Wan,[1,2] Bin Xu,[3] Peng Chen,[4] and Jin-Zhu Zhao[1,2,5,*]

[1]*Guangdong Basic Research Center of Excellence for Structure and Fundamental Interactions of Matter, Guangdong Provincial Key Laboratory of Quantum Engineering and Quantum Materials, School of Physics, South China Normal University, Guangzhou 510006, People's Republic of China*

[2]*Guangdong-Hong Kong Joint Laboratory of Quantum Matter, Frontier Research Institute for Physics, South China Normal University, Guangzhou 510006, People's Republic of China*

[3]*Institute of Theoretical and Applied Physics, Jiangsu Key Laboratory of Thin Films, School of Physical Science and Technology, Soochow University, Suzhou 215006, People's Republic of China*

[4]*Physics Department and Institute for Nanoscience and Engineering, University of Arkansas, Fayetteville, Arkansas 72701, USA*

[5]*Center for Computational Science and Engineering, Southern University of Science and Technology, Shenzhen 518055, People's Republic of China*

(Received 23 June 2023; revised 31 August 2023; accepted 9 October 2023; published 30 October 2023)

A ferroelectric distorted (d) 1*T* (d1*T*)-phase characterized by out-of-plane (OOP) polarization was previously predicted in monolayer transition-metal dichalcogenides, such as MoS_2. A phenomenological model was proposed to explain the centrosymmetric 1*T* (c1*T*)-to-d1*T* transition; however, this model fails to account for polarization reversal. In this work, we reassess the underlying physical origin of spontaneous OOP polarization in the 1*T*-phase of monolayer $MoTe_2$. Through first-principles calculations and the incorporation of a phenomenological model approach utilizing an alternative set of basis states, we confirm that OOP polarization emerges due to its interaction with twofold degenerate, nonpolar primary order parameters. Additionally, we investigate the unique coupling between the polar mode and the primary mode. Notably, employing our newly defined basis sets, we clarify the hybrid improper ferroelectric mechanism, the coupling behavior of lattice modes, phase transitions, and polarization switching within a proposed subspace. Furthermore, our findings highlight that the ferroelectric phase transition can occur even in the absence of unstable phonon modes within the highly symmetric c1*T*-phase, attributed to the higher order coupling between lattice modes.

DOI: 10.1103/PhysRevB.108.165430

I. INTRODUCTION

Two-dimensional (2D) monolayer ferroelectric (FE) materials have garnered significant interest from both experimental and theoretical fields, especially the ones exhibiting out-of-plane (OOP) polarization. These materials hold great promise for miniaturized functional devices [1–4]. In comparison to their three-dimensional (3D) counterparts, 2D ferroelectric materials possess natural layered structures, opening up additional possibilities for ultrathin nanoferroelectric devices [5]. Remarkable advancements have been made through theoretical and experimental investigations, such as the observation of OOP polarization in ultrathin film of $CuInP_2S_6$ [6], in-plane (IP) ferroelectricity in SnTe thin films with atomic thickness [7], the dipole locking between IP and OOP polarization in monolayer In_2Se_3 [8–11], and OOP polarization due to a glide FE mechanism in layered WTe_2 [12–14]. These findings have not only propelled the research progress in the field of 2D ferroelectric materials but have also expanded our understanding of ferroelectric behaviors in diverse materials.

Stable OOP polarization of ultrathin film samples are uncommon in conventional ferroelectric materials. The accumulation of surface charge introduces finite depolarization fields, which usually suppress the spontaneous polarization perpendicular to the surface. According to the modern theory of ferroelectricity, conventional proper ferroelectricity arises from the condensed polar optical phonon mode in the high-symmetry nonpolar reference phase [15]. However, the reduction in total free energy resulting from the condensation of OOP polarization is usually insufficient to withstand the depolarization field [16,17]. Therefore, it is crucial to investigate additional mechanisms beyond the second-order coupling of lattice modes to understand stable OOP polarization in 2D ferroelectric materials. For instance, the interlattice mode coupling beyond the P^2 term plays a vital role in 2D ferroelectric In_2Se_3 [18]. As a representative 2D FE material, monolayer In_2Se_3 exhibits conventional, proper IP ferroelectricity. The higher order coupling between IP and OOP polarization locks these two polarization components and gives rise to spontaneous and reversible OOP polarization.

Similarly, the improper FE [19–22] mechanism with finite OOP polarization in 2D transition-metal dichalcogenides (TMDs) was theoretically proposed in the 1*T*-phase of monolayer MoS_2 [23,24] from theoretical studies, and was also confirmed experimentally in monolayer $MoTe_2$ [25]. In this group of compounds, the OOP polar phonon mode is intrinsically stable while the unstable nonpolar IP motion of the

*zhaojz@m.scnu.edu.cn

molybdenum sublattice, referred to as the K_3 mode, serves as the primary-order parameter driving the FE phase transition. As proposed by first-principles and the phenomenological model [23], OOP polarization in 1*T* MoS_2 is proportional to the square of the K_3 mode, which provides the driving force of the spontaneous polarization. However, several questions still remain unclear due to the complex lattice coupling behavior in these 1*T*-phase TMD monolayers. Specifically, the presence of threefold rotation symmetry results in six energetically equivalent ground states, three of which exhibit opposite directions of OOP polarization compared to the other three. One of the most important issues is how OOP polarization reverses its direction along with the primary-order parameters. As we notice, simply reversing the direction of atomic displacement in the K_3 mode is insufficient to reverse the polarization or to switch to another energetically equivalent state. It implies the presence of complex coupling behaviors in 1*T*-phase TMD monolayers and the necessity for an alternative and comprehensive theoretical description.

In this work, we conducted a series of theoretical investigations focusing on the 1*T*-phase of TMD monolayer $MoTe_2$, where the distorted (d) 1*T*-phase has been experimentally confirmed. Utilizing first-principles calculations, we explored the anharmonic coupling between OOP polarization and nonpolar primary-order parameters. By employing an alternative basis set, we rederived a phenomenological model for the 1*T*-to-d1*T* FE phase transition, considering three equivalent subspaces. These selected subspaces effectively reproduced the first-principles data and provided explicit descriptions of the switching behavior of OOP polarization. Our findings emphasize the significant role of strong higher order coupling effects and a hybrid improper ferroelectric mechanism in governing the structural phase transition in the 1*T*-phase of monolayer $MoTe_2$. Furthermore, we highlight that in a system with an asymmetric potential energy surface (PES), the conventional approach based on soft phonon modes may be insufficient to predict lattice instability accurately. These insights contribute to a deeper understanding of the intricate mechanisms underlying the FE phase transition in monolayer $MoTe_2$.

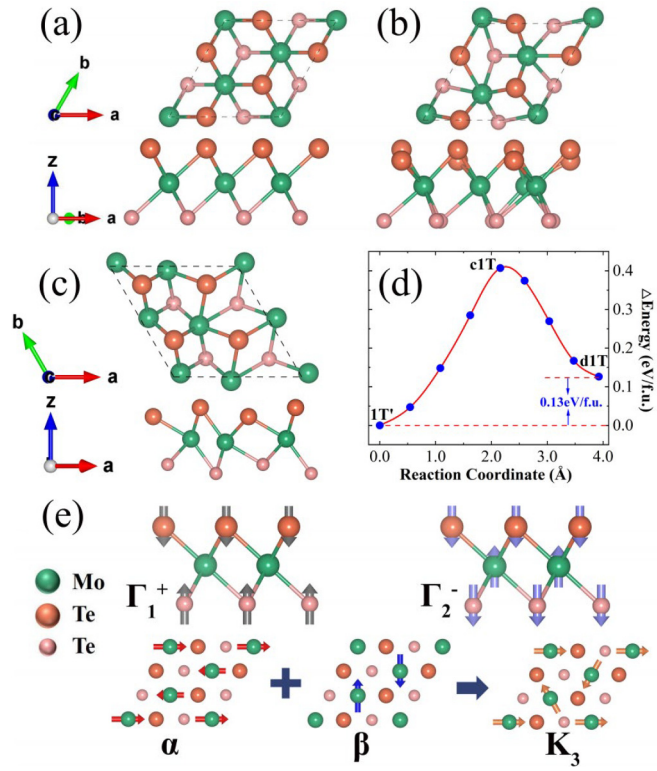

FIG. 1. Schematic diagram of atomic structures and studied phonon modes shown in a $p(\sqrt{3} \times \sqrt{3})$ supercell. (a) The c1*T*-phase of $MoTe_2$, where the $p(1 \times 1)$ formula unit cell is indicated by a dashed line. The green atoms represent the molybdenum atoms, the orange atoms represent the tellurium atoms on the upper layer, and the pink atoms represent the tellurium atoms on the lower layer. (b) The d1*T*-phase of $MoTe_2$. (c) The top view and side view of the atomic structure of the 1*T*′-phase. (d) The energetic barrier of the transition between the 1*T*′- and d1*T*-phase. (e) Vibrational modes of the c1*T*-phase, where eigenvectors are shown by arrows for the modes $Q_{\Gamma_1^+}$, $Q_{\Gamma_2^-}$, Q_α, Q_β, and Q_{K_3}.

II. METHOD

The first-principles calculations were carried out using the Vienna *Ab-initio* Simulation Package [26,27] within the framework of density functional theory (DFT) [28,29]. The electronic exchange-correlation functionals are constructed by the Perdew-Berke-Ernzerhof type of methods in generalized gradient approximation [30–32]. The interaction between ions and electrons is described by the projector-augmented wave method. The orbitals of $4p^6 4d^5 5s^1$ and $5s^2 4p^4$ electrons were explicitly treated as valence states for molybdenum and tellurium, respectively. All atomic positions are fully relaxed until the Hellmann-Feynman force on each atom is less than 10^{-2} eV/Å. The energy cutoff for plane-wave expansion is 550 eV. The 2D Monkhorst-Pack $5 \times 5 \times 1$ *k*-point grid was adopted for the Brillouin zone (BZ) of the unit cell, while the same density of BZ mesh was used for the supercell. *Ab initio* density functional perturbation theory was adopted to study the phonon dispersion curve. The phonon spectrum is calculated using the supercell force-constant approach, while the results of which are analyzed with Phonopy code [33–35]. Setting an ∼15-Å vacuum layer along the *z* direction of the lattice suppresses the interaction between image layers. The group theory analysis of the order parameters is performed using the ISOTROPY [36] package. The electric polarization was calculated using the Berry phase method [37,38].

III. RESULTS AND DISCUSSIONS

A. Coupling between phonon modes

The atomic structure of 1*T*-$MoTe_2$ belongs to the transition-metal chalcogenide hexagonal crystal system. The highly symmetric 1*T* structure of $MoTe_2$ [referred to as centrosymmetric 1*T* (c1*T*)] is shown in Fig. 1(a), and it belongs to the $P\bar{3}\,m1$ space group (No. 164), which has three atomic layers following ABC stacking along OOP direction (referred to as the *z* direction), where the molybdenum layer is in the middle and the two tellurium layers are at the top and bottom. Each tellurium atom forms a Mo-Te tetrahedron with its three nearest neighbor molybdenum atoms. According

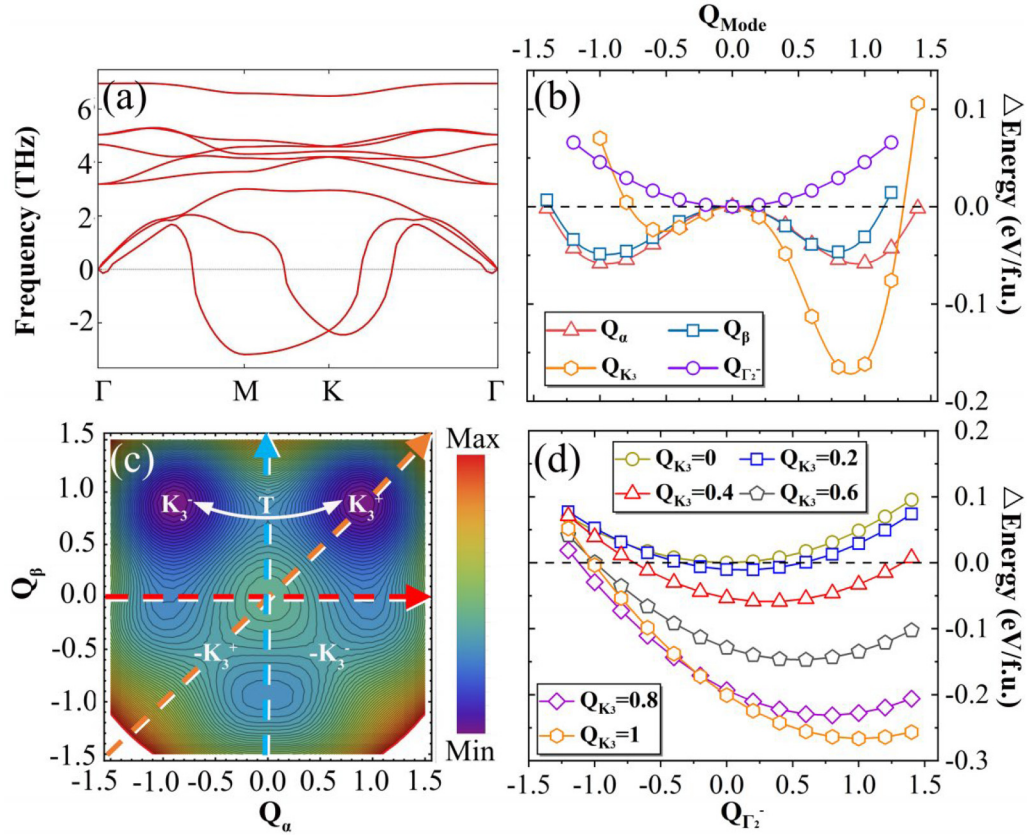

FIG. 2. (a) Phonon dispersion curves of the nonpolar c1T-phase of monolayer $MoTe_2$, where the frequencies of unstable modes are shown in negative values. The selected high-symmetry points in the Brillouin zone are Γ (0, 0, 0), M (0.5, 0, 0), and K ($\frac{2}{3}$, $\frac{1}{3}$, 0). (b) The evolution of the PECs with respect to studied vibrational modes. The red curve corresponds to the Q_α mode, the blue curve corresponds to the Q_β mode, the orange curve refers to the Q_{K_3} distortion combining the Q_α and Q_β modes, and the purple curve refers to the $Q_{\Gamma_2^-}$ mode. (c) The contour diagram of the PES calculated from first-principles calculations projected in the $\{\alpha, \beta\}$ subspace. The depth of color in the figure represents the total free energy of the lattice. (d) The PEC in terms of the $Q_{\Gamma_2^-}$ mode with different amplitudes of Q_{K_3} distortions.

to our calculations, the lattice constant of the three-atom $p(1 \times 1)$ formula unit cell of the c1T-phase is 3.52 Å.

The calculated phonon spectrum, as shown in Fig. 2(a), indicates the lattice instability in the c1T-phase of $MoTe_2$. There are mainly two types of unstable phonon modes observed at the BZ boundary. One mode, located at point M (0.5, 0, 0), primarily corresponds to the transition from the c1T- to the 1T'-phase. The other important unstable modes that appear at point K (1/3, 1/3, 0) are twofold degenerate, which mainly involve two types of in-plane motion of molybdenum atoms with limited tellurium atomic motions. In our work, these two modes are labeled as the Q_α and Q_β modes, and their corresponding eigenvectors are shown in Fig. 1(e). From the projected value in Table I, we can see that the condensation of the Q_α and Q_β modes dominate the distortions of the transition from the c1T- to the d1T-phase. Although there is no lattice instability associated with the phonon mode at point Γ, the modes $Q_{\Gamma_2^-}$ and $Q_{\Gamma_1^+}$, belonging to the Γ_2^- and Γ_1^+ irreducible representations, respectively, are included in the d1T-phase as well. In the subsequent part of our work, we focus on the ferroelectric phase transition from the c1T- to the d1T-phase and the related lattice dynamical behaviors. The optimized lattice constant of the d1T-phase is 3.56 Å, which is in good agreement with the experimental value [25]. In the

TABLE I. The relative energy values of different structures and the projected amplitudes of each phonon vibration mode in the distortion of each phases referring to c1T phase. The 'Fixed lattice' corresponds to the case that the constant of studied phases are fixed at the value of c1T phase. Here the total amplitude of the atomic displacement from c1T to d1T phase is renormalized as the value of 100%.

Free-energy gain (eV/f.u.)			1T'		d1T	
Structure	Fixed lattice	Relaxed lattice	Mode	Amplitude	Mode	Amplitude
c1T	0.00	0.00	X_1^-	92.75%	α	32.93%
d1T	–0.26	–0.29	Γ_1^+	7.25%	β	61.16%
1T'	–0.39	–0.48			Γ_1^+	0.97%
K_3	–0.20	–0.21			Γ_2^-	4.93%

following work, we first suppress the strain effect by fixing the lattice constant at the value of the c1T-phase. As reported in Table I, when the lattice constant is fixed at the value of the c1T-phase, the total energy of the 1T'-phase, the atomic structure of which is shown in Fig. 1(c), is 0.13 eV/f.u. lower than the d1T-phase, indicating the better thermal stability of the 1T'-phase. However, further studies show that there is an ~0.26 eV/f.u. energy barrier when the structure transforms from d1T to 1T', as shown in Fig. 1(d), which may explain the experimental observation of the d1T-phase on the hexagonal substrates [25].

The atomic distortions from c1T to d1T can be divided into two groups. As shown in Fig. 1(e), the first group includes two types of motion contributed by the $Q_{\Gamma_2^-}$ and $Q_{\Gamma_1^+}$ modes, corresponding to the phonon modes at the BZ center without any supercell modulation. Among these two modes, OOP polarization directly comes from the condensation of the $Q_{\Gamma_2^-}$ mode, which brings the polar type of OOP atomic motion.

The $Q_{\Gamma_1^+}$ mode relates to the nonpolar motion along the z direction, the condensation of which does not alter the symmetry of the lattice. We therefore ignore the $Q_{\Gamma_1^+}$ mode in the following work. The second group of distortions induces the structural modulation of the supercell and relates to the K_3 irreducible representation, as illustrated in Fig. 1(e). This Q_{K_3} distortion contains the IP trimerization of molybdenum atoms, accompanied by the IP motion of tellurium atoms in the bottom layer, as well as the OOP motion of tellurium atoms in the top layer. Such Q_{K_3} distortion arises from the combined atomic motion of the Q_α mode and Q_β mode, which are depicted in Fig. 1(e).

By tracing the evolution of the total energy with respect to the amplitude of each individual phonon mode, we observe the typical double-well energy curve for the Q_α and Q_β modes, and a single-well curve for the $Q_{\Gamma_2^-}$ mode. As shown in Fig. 2(b), the potential energy curves (PECs) confirm the instabilities of the Q_α and Q_β modes, as well as the stable $Q_{\Gamma_2^-}$ mode. Both curves for Q_α and Q_β exhibit similar negative curvature around the origin point (reference structure), which are in agreement with their degenerate vibrational frequencies. Furthermore, the combination of Q_α and Q_β can yield the Q_{K_3} mode, which further reduces the total energy, resulting in an asymmetric double-well curve. The details of how the combination of the Q_α and Q_β modes produces Q_{K_3} distortions are illustrated in Supplemental Material Fig. S1 [39]. Consequently, the condensation of the individual Q_α and Q_β modes reduces the total energy by 0.06 eV/f.u. and 0.05 eV/f.u. per supercell, respectively, while it will reduce more than 0.16 eV/f.u. when the Q_α and Q_β modes condense together. The minimum of the Q_{K_3} curve, located on the right side of the orange line in Fig. 2(b), where the inversion symmetry is broken, belongs to the $P31m$ (No. 157) space group.

We plot the free-energy surface with respect to the Q_α and Q_β modes, as depicted in Fig. 2(c). The energy evolution paths swept by the red, blue, and orange dashed lines correspond to the potential energy curves of the same color in Fig. 2(b). It is clearly evident that there are two energetically twofold minimum points, referred as the K_3^+ ($Q_\alpha = 1$, $Q_\beta = 1$) and K_3^- ($Q_\alpha = -1$, $Q_\beta = 1$) states, both of which belong to the same space group. By reversing the sign of Q_α while keeping $Q_\beta = 1$, the lattice can be switched between these two minimum points.

Upon further relaxation of the atomic positions from the K_3^+ and K_3^- states while constraining the symmetry, the condensation of the $Q_{\Gamma_2^-}$ mode is automatically induced, resulting in the ground-state FE d1T-phase. This d1T-phase presents 0.44 μC/cm^2 OOP polarization and has a total energy that is 0.26 eV/f.u. lower than the reference c1T-phase. It is noteworthy that the K_3^+ and K_3^- structures have opposite directions of OOP polarization.

There is no lattice instability for the $Q_{\Gamma_2^-}$ mode, while the coexistence of the Q_α and Q_β modes determines the symmetry of the ground-state d1T-phase. The absence of lattice instability in the $Q_{\Gamma_2^-}$ mode confirms its role as a secondary-order parameter, coupled to the Q_{K_3} distortion. The results in Fig. 2(d) provide further confirmation that the condensation of the $Q_{\Gamma_2^-}$ mode strongly relies on the amplitude of the Q_{K_3} distortion while maintaining its single-well curve. Thus, a combination of the Q_α and Q_β modes acts as the primary-order parameter, causing the minimum point of the single-energy well for the $Q_{\Gamma_2^-}$ mode to move from the origin point to a point with a finite OOP value, thereby generating OOP polarization.

The energetically preferred switching path in PESs between the K_3^+ and K_3^- states [indicated by the white double-headed arrow in Fig. 2(c)] does not pass through the reference c1T-phase. Instead, it keeps the Q_β mode with a finite value. It is further confirmed by nudged elastic band (NEB) calculations, as shown in Fig. 3(a), where the transition state has an energy of ~0.19 eV/f.u. higher than the d1T-phase with a finite amplitude of the condensed Q_β mode.

It is worth noting that the $\{\alpha, \beta\}$ subspace is threefold due to the hexagonal symmetry of the lattice. Thus, the complete description of the PES is given by $\{\alpha_i, \beta_i\}_i$ ($i = 1, 2, 3$), representing threefold α_i modes and threefold β_i modes connected by threefold rotation along the z-axis, respectively (see Supplemental Material Fig. S2 [39]). In each subspace, there are two energy minima with opposite directions of OOP polarization. Therefore, the system possesses six energetically equivalent ground states, three of which have positive OOP polarization while the other three have negative OOP polarization [see Fig. 3(c)].

During the transition from the high-symmetry c1T-phase [point O in Fig. 3(c)], the lattice has an equal probability of entering each subspace. As shown in Fig. 3(a), when the direction of OOP polarization is switched between the B and C states within individual subspace II, the β_2 mode, belonging to the same subspace, is presented in the transition state $T(\beta_2)$ [see Fig. 3(a) and the solid blue line in Fig. 3(c)]. Conversely, when OOP polarization is switched between two subspaces—for instance, between points A and B belonging to subspaces III and II, respectively, the transition state will only condense the Q_{β_1} mode belonging to subspace I [see Fig. 3(b) and the dashed blue line in Fig. 3(c)]. Since the transition state T with a finite Q_β mode is threefold energetically, it is implied that the lattice may have the same possibilities to go into each

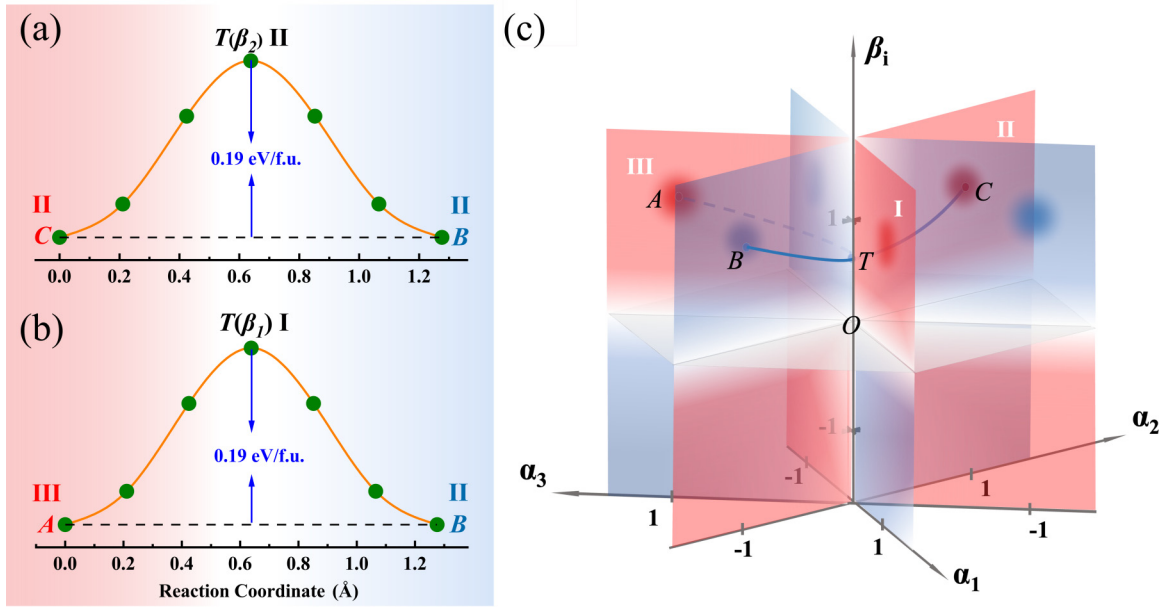

FIG. 3. The energy evolution of the OOP polarization switching path, calculated using the NEB method, between (a) point B ($Q_{\alpha_2} = -1$, $Q_{\beta_2} = 1$) and point C ($Q_{\alpha_2} = 1$, $Q_{\beta_2} = 1$) in subspace II, and (b) the path between point A ($Q_{\alpha_3} = 1$, $Q_{\beta_3} = 1$) and point B ($Q_{\alpha_2} = -1$, $Q_{\beta_2} = 1$) between subspaces II and III. The transition states of these two paths and the energy barriers are highlighted. The red and blue backgrounds refer to the positive and negative directions of OOP polarization, respectively; white refers to nonpolar states. (c) The schematic plots of subspaces I, II, and III correspond the basis α_i and β_i, where the value of i can be 1, 2, and 3, respectively. The β_i-axis is threefold. The regions that present positive and negative directions of OOP polarization are in red and blue, respectively. White corresponds to nonpolar states. The six energetically equivalent ground states, corresponding to $Q_{\alpha_i} = 1$ and $Q_{\beta_i} = 1$ are marked by fuzzy red and blue circles. Two phase transition paths, the ones from A to B, are highlighted by dashed and solid blue lines, respectively. The threefold transition states with a suppressed Q_{α_i} mode are marked as point T on the β_i-axis.

individual subspace when switching the direction of OOP polarization.

B. Phenomenological model of free-energy expansion

To understand the coupling between relevant lattice modes more completely, we here employ a phenomenological approach by expanding the free energy in terms of the corresponding order parameters. We first consider the modes' contribution in a single $\{\alpha, \beta\}$ subspace. As described in Eq. (1), the free energy consists of two main contributions: the contribution of the individual Q_α and Q_β modes, and the coupling between them:

$$f\{\alpha, \beta\} = \kappa_{11}Q_\alpha^2 + \kappa_{12}Q_\alpha^4 + \kappa_{21}Q_\beta^2 + \kappa_{22}Q_\beta^3 + \kappa_{23}Q_\beta^4 + \lambda_1 Q_\alpha^2 Q_\beta + \lambda_2 Q_\alpha^2 Q_\beta^2. \quad (1)$$

The first five terms of Eq. (1) represents the double-well PEC of the individual Q_α and Q_β modes. These two degenerate orthogonal modes share the same imaginary frequency, leading to the same coefficient for the Q_α^2 and Q_β^2 terms. Additionally, considering the slight asymmetry of the PEC for the Q_β mode, we include a Q_β^3 term in the model. However, the amplitude of the coefficient associated with Q_β^3 is small compared to the other terms.

The last two terms in Eq. (1) capture the coupling effect between the Q_α and Q_β modes. By examining the values reported in Table II, we observe a significant asymmetric coupling effect, as indicated by the $Q_\alpha^2 Q_\beta$ term. In contrast, the repulsive effect between the Q_α and Q_β modes, represented by the $Q_\alpha^2 Q_\beta^2$ term, is relatively weak. Despite the truncation of the expansion at the fourth order as an approximation, Eq. (1) successfully reproduces the corresponding PES data obtained from first-principles calculations, as demonstrated in Supplemental Material Fig. S3(a) [39]. It is confirmed that the coupling between the Q_α and Q_β modes leads to the emergence of the K_3^+ and K_3^- states as the minima in the $\{\alpha, \beta\}$ subspace.

In Figs. 4(a) and 4(b), we show the PECs for the individual Q_α and Q_β modes. These PECs are in excellent agreement with the data obtained from first-principles calculations. It is observed that the Q_α mode shows symmetric double-well PECs for different amplitudes of the Q_β mode. On the other hand, the asymmetric behavior for the PEC of the Q_β mode

TABLE II. The value of each coefficient parameter in the Landau model of Eqs. (1) and (2) in the absence of strain.

Coefficient	Value	Coefficient	Value
κ_{11}	–0.411	χ_1	0.277
κ_{12}	0.264	χ_2	–0.007
κ_{21}	–0.400	χ_3	0.137
κ_{22}	–0.066	χ_4	0.037
κ_{23}	0.317	χ_5	–0.006
λ_1	–0.176	χ_6	0.000
λ_2	0.088		

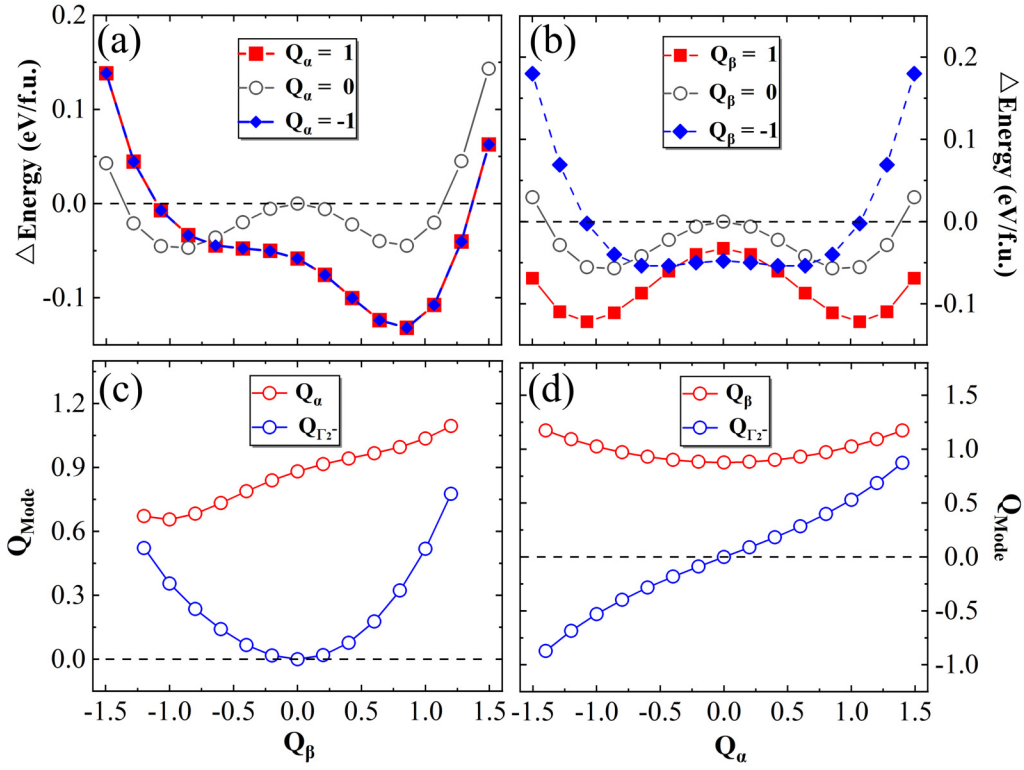

FIG. 4. The investigated PECs in terms of different modes in an individual 2D $\{\alpha, \beta\}$ subspace. (a) The evolution of the PEC in terms of the Q_β mode under a fixed amplitude of the Q_α mode. (b) The evolution of the PEC in terms of the Q_α mode under a fixed amplitude of the Q_β mode. The investigated PECs in terms of different modes in an individual 3D $\{\alpha, \beta, \Gamma_2^-\}$ subspace. (c) The evolution of the PECs for the absolute value of the Q_α and $Q_{\Gamma_2^-}$ modes in terms of the amplitude of the Q_β mode. (d) The evolution of the PECs for the Q_β and $Q_{\Gamma_2^-}$ modes in terms of the amplitude of the Q_α mode.

becomes significant under a finite value of the Q_α mode. Overall, the condensation of the Q_{K_3} distortion, equivalent to the combination of the Q_α and Q_β modes, can be considered as an energetical preference of the lattice, rather than being solely dictated by symmetry confinement.

When the energy expansion is considered in three dimensional $\{\alpha, \beta, \Gamma_2^-\}$ subspace, the contribution of the $Q_{\Gamma_2^-}$ mode to the energy can be expressed as shown in Eq. (2):

$$F\{\alpha, \beta, \Gamma_2^-\} = f\{\alpha, \beta\} + Q_{\Gamma_2^-}\left(\chi_1 Q_\alpha Q_\beta^2 + \chi_2 Q_\alpha^3\right) + Q_{\Gamma_2^-}^2\left(\chi_3 + \chi_4 Q_\alpha^2 + \chi_5 Q_\beta^2\right) + \chi_6 Q_{\Gamma_2^-}^4. \quad (2)$$

This expression incorporates terms involving the $Q_{\Gamma_2^-}$ mode itself, as well as coupling terms between the three relevant modes. By examining the values of each coefficient parameter (provided in Table II), we observe that the energy dependence follows a harmonic behavior concerning the $Q_{\Gamma_2^-}$ mode, rendering the fourth-order terms negligible. Moreover, due to this observation, both the coupling term between the third order of the Q_α mode (Q_α^3) and the linear $Q_{\Gamma_2^-}$ mode, as well as the biquadratic term $Q_{\Gamma_2^-}^2 Q_\beta^2$, can be considered energetically insignificant.

In the Taylor expansion within the $F\{\alpha, \beta, \Gamma_2^-\}$ framework, we observe additional biquadratic terms that correspond to the repulsive effect between the $Q_{\Gamma_2^-}$ and Q_α modes. Furthermore, there exists a linear coupling between the polar $Q_{\Gamma_2^-}$ mode and the combination of the Q_α and Q_β modes ($Q_\alpha Q_\beta^2 Q_{\Gamma_2^-}$). This coupling plays a pivotal role in generating OOP polarization. It can be further revealed by minimization of the free energy according to $\frac{\partial F}{\partial P} = 0$, by which the dependence relation between the secondary $Q_{\Gamma_2^-}$ mode and primary modes can be described as

$$Q_{\Gamma_2^-} = -\frac{1}{2}\frac{\chi_1 Q_\alpha Q_\beta^2}{\chi_3 + \chi_4 Q_\alpha^2}. \quad (3)$$

This coupling mechanism is also clearly illustrated in Figs. 4(c) and 4(d).

Notably, the presence of a finite $Q_{\Gamma_2^-}$ mode relies on the condensation of the primary Q_α and Q_β modes. These interactions and couplings between the modes form the central mechanism driving the emergence of OOP polarization. Thus, if either of these two modes is suppressed, $Q_{\Gamma_2^-}$ is eliminated. The curves shown in Figs. 4(c) and 4(d) indicate that the amplitude of $Q_{\Gamma_2^-}$ can be estimated to be linearly dependent on the Q_α mode and proportional to the second-order term of the Q_β mode, being in agreement with Eq. (3).

So far, we can see the secondary $Q_{\Gamma_2^-}$ is essentially dependent on the Q_α and Q_β modes. It is interesting to investigate how OOP polarization depends on the amplitude of the Q_{K_3} mode. Here, the amplitude of $Q_{\Gamma_2^-}$ is approximately estimated as $Q_{\Gamma_2^-} \propto -\frac{1}{2}\frac{\chi_1 |Q_{K3}^3|}{\chi_3 + \chi_4 Q_{K3}^2}$, assuming that Q_α and Q_β condense with the same amplitude. As we show in Supplemental

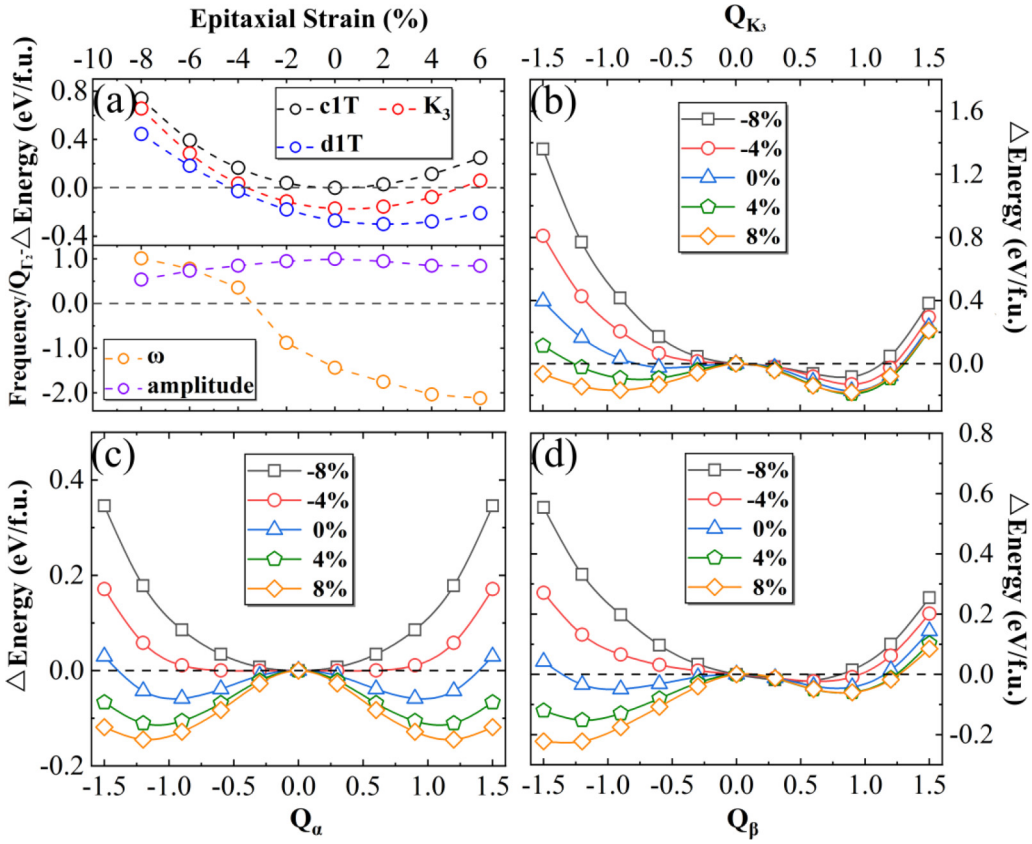

FIG. 5. The evolution of related physical quantities under the effect of epitaxial strain. (a) The PECs of the c1*T*-phase, d1*T*-phase, and Q_{K_3} state with respect to the epitaxial strain are reported in the top panel. In the bottom panel, the twofold energetic frequencies of the Q_α and Q_β modes, and the amplitude of $Q_{\Gamma_2^-}$ in the d1*T*-phase in terms of epitaxial strain are shown. Here, the maximum value of frequency ($\omega = 2.0$ THz) is normalized to 1.0, while the values of the rest of the points are reported accordingly. The evolution of the PECs referring to the c1*T*-phase of $MoTe_2$ in terms of the Q_{K_3} distortion (b), the Q_α mode (c), and the Q_β mode (d) with respect to epitaxial strain.

Material Fig. S3(b) [39], this approximation provides a qualitatively good fit to the data obtained from first-principles calculations when the parameters are appropriately adjusted, particularly for large values of Q_{K_3}, where the amplitude of the $Q_{\Gamma_2^-}$ mode exhibits a linear dependence on Q_{K_3}. However, it is important to note that simply reversing the sign of Q_{K_3} will not reverse the polarization.

It is worthwhile to discuss the relation between the $\{\alpha, \beta\}$ representation and the proposed primary Q_{K_3} mode approach [23]. Our work confirmed that coexistence of the Q_α and Q_β modes is not constrained by symmetry. Both of them can condense in the c1*T*-phase individually. The appearance of the Q_{K_3} distortion is the energetical preference of the lattice that combines the Q_α and Q_β modes, rather than symmetry. This argument is supported by the fact that the preferred pathway in the PES for reversing the direction of OOP polarization does not go through the reference c1*T* state but with finite value of Q_β. OOP polarization relating the $Q_{\Gamma_2^-}$ mode is strictly locked to the combination of the Q_α and Q_β modes. In other words, the precondition of a finite $Q_{\Gamma_2^-}$ mode is the coexistence of the Q_α and Q_β modes. Therefore, since OOP polarization arises from two modes with different symmetries, the phase transition from c1*T* to d1*T* should be considered hybrid improper ferroelectricity [40,41].

C. Transition in the absence of unstable phonon modes

As we discussed earlier, the high-order coupling between the Q_α and Q_β modes dominates the phase transition. Such a central mechanism does not necessarily rely on the soft phonon modes, which can be further highlighted and can introduce remarkable phenomena under biaxial in-plane strain. When compressive strain is applied, the phonon instabilities at point *K* of the c1*T*-phase becomes weak. The positive value corresponds to tensile strain while the negative ones correspond to compressive strain. In Fig. 5(a), the imaginary frequency disappears when the amplitude of the compressive strain reaches more than ∼3%. However, even in the range of –8% to –6% strain, the free energy of the d1*T*-phase remains lower than that of the c1*T*-phase, coinciding with the finite OOP values [see Fig. 5(a)]. The corresponding electronic band structures of d1*T*-phase and c1*T*-phase are reported in Supplemental Material Figs. S4–S5 [39]. These indicate that the FE phase transition is not solely dependent on the existence of the imaginary phonon frequency of the primary-order parameters. This observation is further confirmed when detailed studies are performed on the evolution of the PES with respect to in-plane strain. As shown in Figs. 5(c) and 5(d), the negative curvature of the PEC in terms of the Q_α and Q_β modes is enhanced under tensile strain, and continuously

changes to a positive curvature when compressive strain is applied. The critical point is between –3% and –4%, at which the curvature coincides with the disappearance of unstable phonon frequencies. It is important to note that the harmonic approximation is valid only in the narrow region close to the origin point, particularly for the Q_β mode, which exhibits an asymmetric PEC when its amplitude is large. When the negative curvature disappears, the PEC for the individual Q_α and Q_β modes becomes a single-well type. The minimum point for the Q_α mode is at the origin, while the one for the Q_β mode is slightly away from the origin point.

Such asymmetric behavior in the PEC with respect to Q_{K_3} distortion is significantly enhanced. This PEC leads to the spontaneous transition of the lattice from c1T to d1T, even in the absence of the unstable phonon mode. This phenomenon confirms that the FE transition in $MoTe_2$ is dominated by the high-order coupling of lattice modes, resulting in a robust OOP polarization under a depolarization field. Furthermore, these findings also suggest that the estimation of lattice stability via harmonic approximation may not be reliable, as the system exhibits a strong, asymmetric PES. This behavior can be further confirmed by the phenomenological model. In Eq. (1), when we gradually change the coefficient parameters of the harmonic Q_α^2 and Q_β^2 terms from negative values to zero or even positive values, the d1T-phase remains lower in energy than the reference c1T-phase, indicating a maintained FE phase transition (see Supplemental Material Fig. S6 [39]).

IV. CONCLUSION

We have conducted a comprehensive investigation of the FE phase transition of the monolayer $MoTe_2$ from the c1T-phase to the d1T-phase. Through first-principles calculations, we obtained the PES, which reveals the intricate coupling of the lattice modes during the transition. Our analysis of the DFT data demonstrated that the previously proposed Q_{K_3} mode, involving an in-plane displacement, can be alternatively projected in the $\{\alpha, \beta\}$ subspace. Furthermore, we clarified that OOP polarization in the d1T-phase arises from hybrid improper ferroelectricity. To understand more completely the contribution of these phonon modes to ferroelectric phase transition, we developed a phenomenological model. This model provides insights into the high-order coupling between the Q_α and Q_β modes, and its impact on ferroelectric properties. It allows us to demonstrate clearly the underlying mechanisms governing the phase transition. This mechanism is further highlighted when biaxial strain is applied to the system. We observed the disappearance of the imaginary phonon frequency under compressive strain, while the potential well associated with the ferroelectric phase remained. Overall, our study provides a comprehensive understanding of the ferroelectric phase transition in the 1T-phase of monolayer $MoTe_2$, shedding light on the complex lattice dynamics and on the role of high-order mode couplings. These findings contribute to the broader knowledge of ferroelectric materials and their potential applications in electronic devices.

ACKNOWLEDGMENTS

This work was financially supported by the National Natural Science Foundation of China (Grant No. 12274145), Guangdong Basic and Applied Basic Research Foundation, China (Grant No. 2023A1515010672), Guangdong Provincial University Science and Technology Program (Grant No. 2023KTSCX029). Bin Xu acknowledges financial support from National Natural Science Foundation of China under Grant No. 12074277. J.-Z. Zhao acknowledges the startup funding from South China Normal University.

[1] T. Birol, Stable and switchable polarization in 2D, Nature (London) **560**, 174 (2018).

[2] K. S. Novoselov, A. Mishchenko, A. Carvalho, and A. H. Castro Neto, 2D materials and van der Waals heterostructures, Science **353**, aac9439 (2016).

[3] K. Yamauchi and P. Barone, Electronic ferroelectricity induced by charge and orbital orderings, J. Phys. Condens. Matter **26**, 103201 (2014).

[4] A. Lipatov, P. Chaudhary, Z. Guan, H. Lu, G. Li, O. Crégut, K. D. Dorkenoo, R. Proksch, S. Cherifi-Hertel, D.-F. Shao, E. Y. Tsymbal, J. Íñiguez, A. Sinitskii, and A. Gruverman, Direct observation of ferroelectricity in two-dimensional MoS_2, npj 2D Mater. Appl. **6**, 18 (2022).

[5] J. Junquera and P. Ghosez, Critical thickness for ferroelectricity in perovskite ultrathin films, Nature (London) **422**, 506 (2003).

[6] F. Liu, L. You, K. L. Seyler, X. Li, P. Yu, J. Lin, X. Wang, J. Zhou, H. Wang, H. He, S. T. Pantelides, W. Zhou, P. Sharma, X. Xu, P. M. Ajayan, J. Wang, and Z. Liu, Room-temperature ferroelectricity in $CuInP_2S_6$ ultrathin flakes, Nat. Commun. **7**, 12357 (2016).

[7] K. Chang, J. Liu, H. Lin, N. Wang, K. Zhao, A. Zhang, F. Jin, Y. Zhong, X. Hu, W. Duan, Q. Zhang, L. Fu, Q.- K. Xue, X. Chen, and S.- H. Ji, Discovery of robust in-plane ferroelectricity in atomic-thick SnTe, Science **353**, 274 (2016).

[8] Y. Zhou, D. Wu, Y. Zhu, Y. Cho, Q. He, X. Yang, K. Herrera, Z. Chu, Y. Han, M. C. Downer, H. Peng, and K. Lai, Out-of-plane piezoelectricity and ferroelectricity in layered α-In_2Se_3 nanoflakes, Nano Lett. **17**, 5508 (2017).

[9] C. Cui, W.- J. Hu, X. Yan, C. Addiego, W. Gao, Y. Wang, Z. Wang, L. Li, Y. Cheng, P. Li, X. Zhang, H. N. Alshareef, T. Wu, W. Zhu, X. Pan, and L.- J. Li, Intercorrelated in-plane and out-of-plane ferroelectricity in ultrathin two-dimensional layered semiconductor In_2Se_3, Nano Lett. **18**, 1253 (2018).

[10] W. Ding, J. Zhu, Z. Wang, Y. Gao, D. Xiao, Y. Gu, Z. Zhang, and W. Zhu, Prediction of intrinsic two-dimensional ferroelectrics in In_2Se_3 and other III_2-VI_3 van der Waals materials, Nat. Commun. **8**, 14956 (2017).

[11] J. Xiao, H. Zhu, Y. Wang, W. Feng, Y. Hu, A. Dasgupta, Y. Han, Y. Wang, D. A. Muller, L. W. Martin, P. Hu, and X. Zhang, Intrinsic two-dimensional ferroelectricity with dipole locking, Phys. Rev. Lett. **120**, 227601 (2018).

[12] P. Sharma, F.- X. Xiang, D.- F. Shao, D. Zhang, E. Y. Tsymbal, A. R. Hamilton, and J. Seidel, A room-temperature ferroelectric semimetal, Sci. Adv. **5**, eaax5080 (2019).

[13] Z. Fei, W. Zhao, T. A. Palomaki, B. Sun, M. K. Miller, Z. Zhao, J. Yan, X. Xu, and D. H. Cobden, Ferroelectric switching of a two-dimensional metal, Nature (London) **560**, 336 (2018).

[14] Q. Yang, M. Wu, and J. Li, Origin of two-dimensional vertical ferroelectricity in WTe_2 bilayer and multilayer, J. Phys. Chem. Lett. **9**, 7160 (2018).

[15] M. E. Lines and A. M. Glass, *Principles and Applications of Ferroelectrics and Related Materials* (Oxford University Press, New York, 2001).

[16] P. Ghosez and J. Junquera, in *Handbook of Theoretical and Computational Nanotechnology*, edited by M. Rieth, and W. Schommers (American Scientific, Stevenson Ranch, 2006).

[17] Y. Watanabe, Appropriate value of permittivity for depolarization field and universal instability of insulating ferroelectric phase in single-domain state, Ferroelectrics **406**, 35 (2010).

[18] W.-J. Shuai, R. Wang, and J.-Z. Zhao, Ferroelectric phase transition driven by anharmonic lattice mode coupling in two-dimensional monolayer In_2Se_3, Phys. Rev. B **107**, 155427 (2023).

[19] A. P. Levanyuk and D. G. Sannikov, Improper ferroelectrics, Sov. Phys. Usp. **17**, 199 (1974).

[20] C. J. Fennie and K. M. Rabe, Ferroelectric transition in $YMnO_3$ from first principles, Phys. Rev. B **72**, 100103(R) (2005).

[21] B. B. Van Aken, T. T. M. Palstra, A. Filippetti, and N. A. Spaldin, The origin of ferroelectricity in magnetoelectric $YMnO_3$, Nat. Mater. **3**, 164 (2004).

[22] E. Bousquet, M. Dawber, N. Stucki, C. Lichtensteiger, P. Hermet, S. Gariglio, J.-M. Triscone, and P. Ghosez, Improper ferroelectricity in perovskite oxide artificial superlattices, Nature (London) **452**, 732 (2008).

[23] S. N. Shirodkar and U. V. Waghmare, Emergence of ferroelectricity at a metal-semiconductor transition in a 1*T* monolayer of MoS_2, Phys. Rev. Lett. **112**, 157601 (2014).

[24] J.-H. Choi and S.-H. Jhi, Origin of robust out-of-plane ferroelectricity in $d1T$-MoS_2 monolayer, J. Phys. Condens. Matter **32**, 045702 (2020).

[25] S. Yuan, X. Luo, H. L. Chan, C. Xiao, Y. Dai, M. Xie, and J. Hao, Room-temperature ferroelectricity in $MoTe_2$ down to the atomic monolayer limit, Nat. Commun. **10**, 1775 (2019).

[26] G. Kresse and J. Furthmüller, Efficient iterative schemes for *ab initio* total-energy calculations using a plane-wave basis set, Phys. Rev. B **54**, 11169 (1996).

[27] G. Kresse and J. Hafner, *Ab initio* molecular dynamics for open-shell transition metals, Phys. Rev. B **48**, 13115 (1993).

[28] P. Hohenberg and W. Kohn, Inhomogeneous electron gas, Phys. Rev. **136**, B864 (1964).

[29] W. Kohn and L. J. Sham, Self-consistent equations including exchange and correlation effects, Phys. Rev. **140**, A1133 (1965).

[30] J. P. Perdew, K. Burke, and M. Ernzerhof, Generalized gradient approximation made simple, Phys. Rev. Lett. **77**, 3865 (1996).

[31] J. P. Perdew, K. Burke, and M. Ernzerhof, Generalized gradient approximation made simple [Phys. Rev. Lett. **77**, 3865 (1996)], Phys. Rev. Lett. **78**, 1396 (1997).

[32] Y. Zhang and W. Yang, Comment on "generalized gradient approximation made simple," Phys. Rev. Lett. **80**, 890 (1998).

[33] A. Togo and I. Tanaka, First principles phonon calculations in materials science, Scr. Mater. **108**, 1 (2015).

[34] A. Togo, First-principles phonon calculations with phonopy and Phono3py, J. Phys. Soc. Jpn. **92**, 012001 (2023).

[35] A. Togo, L. Chaput, T. Tadano, and I. Tanaka, Implementation strategies in phonopy and phono3py, J. Phys. Condens. Matter **35**, 353001 (2023).

[36] H. T. Stokes, D. M. Hatch, and B. J. Campbell, ISOTROPY software suite, iso.byu.edu.

[37] R. D. King-Smith and D. Vanderbilt, Theory of polarization of crystalline solids, Phys. Rev. B **47**, 1651 (1993).

[38] N. A. Spaldin, A beginner's guide to the modern theory of polarization, J. Solid State Chem. **195**, 2 (2012).

[39] See Supplemental Material at http://link.aps.org/supplemental/10.1103/PhysRevB.108.165430 for (i) superpositions of unstable phonon modes and the corresponding eigenvectors, (ii) the potential energy surface and the evolution of out-of-plane polarization with respect to in-plane modes, (iii) the band structures of the d1T-phase and the c1T-phase sequentially under different epitaxial strain, (iv) the potential energy curves of the model under different amplitudes of epitaxial strain, and (v) mode amplitudes of intermediate states.

[40] N. A. Benedek and C. J. Fennie, Hybrid improper ferroelectricity: A mechanism for controllable polarization-magnetization coupling, Phys. Rev. Lett. **106**, 107204 (2011).

[41] N. A. Benedek and M. A. Hayward, Hybrid improper ferroelectricity: A theoretical, computational, and synthetic perspective, Annu. Rev. Mater. Res. **52**, 331 (2022).